JGR Atmospheres

RESEARCH ARTICLE
10.1029/2021JD035577

Life Cycle of Shallow Marine Cumulus Clouds From Geostationary Satellite Observations

Torsten Seelig[1], Hartwig Deneke[2], Johannes Quaas[1], and Matthias Tesche[1]

[1]Leipzig Institute for Meteorology (LIM), University Leipzig, Leipzig, Germany, [2]Leibniz Institute for Tropospheric Research (TROPOS), Leipzig, Germany

Key Points:

- The life cycle of shallow marine cumulus clouds is inferred using a passive space-based geostationary instrument
- Life cycle is quantified by top temperature/height, cloud extent, cloud water path, optical thickness, and droplet radius/number concentration
- Cumulus clouds of a certain horizontal extent, cloud top height as well as droplet radius live longer if they are optically denser

Correspondence to:
T. Seelig,
seelig@uni-leipzig.de

Citation:
Seelig, T., Deneke, H., Quaas, J., & Tesche, M. (2021). Life cycle of shallow marine cumulus clouds from geostationary satellite observations. *Journal of Geophysical Research: Atmospheres*, *126*, e2021JD035577. https://doi.org/10.1029/2021JD035577

Received 16 JUL 2021
Accepted 28 OCT 2021

Author Contributions:
Conceptualization: Torsten Seelig, Matthias Tesche
Formal analysis: Torsten Seelig
Funding acquisition: Matthias Tesche
Investigation: Torsten Seelig
Methodology: Torsten Seelig
Project Administration: Matthias Tesche
Resources: Hartwig Deneke
Software: Torsten Seelig
Writing – original draft: Torsten Seelig, Matthias Tesche
Writing – review & editing: Hartwig Deneke, Johannes Quaas, Matthias Tesche

Abstract An analysis of the life cycle of shallow marine cumulus clouds is presented based on geostationary observations by the Spinning Enhanced Visible and InfraRed Imager aboard Meteosat Second Generation (MSG-SEVIRI). Trajectories of about 250,000 individual shallow marine cumulus clouds have been derived by applying Particle Image Velocimetry to the Satellite Application Facility on Climate Monitoring CLoud property dAtAset using SEVIRI for a region in the trade wind zone centered around the Canary Islands in August 2015. The temporal evolution of the physical properties of these clouds allows to characterize cloud development and to infer the distribution of cloud life time and cloud extent. In the derived data set, the life time distribution follows a double power law with most clouds existing on a time scale of tens of minutes. The cloud physical properties, available during daytime, are analyzed along the cloud tracks. Relative time series of cloud extent, cloud water path, cloud droplet effective radius at cloud top, cloud optical thickness, and cloud droplet number concentration for clouds in two temporal ranges reveal conditions that can be attributed to long-lasting clouds. Clouds of a certain horizontal extent and cloud top height as well as cloud droplet radius show longer life times if they are optically more dense, i.e., have a higher droplet number concentration. Furthermore, the investigation of the content of liquid cloud water regarding cloud life time and cloud extent shows that small short-living clouds significantly contribute to cloud radiative effects.

Plain Language Summary A comprehensive analysis of the life cycle of shallow marine cumulus clouds is presented based on measurements of a specialized instrument, called SEVIRI, aboard Meteosat's Second Generation geostationary meteorological satellite. A new method is applied to derive the physic-property temporal evolution of approximately 250,000 individual clouds in a region around the Canary Islands during August 2015. Several constraints are applied to infer the relationship between cloud life time and various cloud parameters. The study reveals that cloud life time is related to the optical thickness when constrained by horizontal extent, cloud top height, and droplet radius. The analysis further shows that small short-living clouds significantly contribute to cloud radiative effects.

1. Introduction

Clouds and their interaction with short- and long-wave radiation mark one of the major uncertainties in our quantification of the Earth's energy budget and our understanding of climate change (Boucher et al., 2013). Bright low-level clouds are of particular importance in modulating planetary albedo. They occur over cooler subtropical oceans or in polar regions (Mace et al., 2009; Stubenrauch et al., 2013). They are less common over land, especially during the day and in winter (Chepfer et al., 2010; Mace et al., 2009). Shallow (low-level) clouds are prevalent in nearly all types of convective systems and their occurrence is underestimated by models (Berry et al., 2020; Chepfer et al., 2008; Haynes et al., 2011; Naud et al., 2010; Tselioudis et al., 2021; Vignesh et al., 2020). Common types of clouds within the planetary boundary layer are stratiform (non-convective) and cumuliform (convective). The transition between types is classified to be stratocumuliform. Stratus clouds producing a uniform gray layer of cloud cover show a global-average cloud fraction of approximately 5%–15% (Eastman et al., 2011) while shallow cumulus clouds show an average cloud fraction of approximately 5%–30% (Mieslinger et al., 2019). Shallow cumulus clouds organized as bands, clusters, and isolated scattered cells (Nuijens et al., 2009) occur persistently year-round over marine terrain (Eastman et al., 2011). Typical sizes of shallow cumulus clouds range over several scales (Heus & Seifert, 2013) and they are responsible for the transport of temperature, moisture, and momentum through the boundary layer (Grant & Lock, 2004). In the cloud layer, on the one hand, shallow cumulus clouds are the source of con-

vection, turbulence, and (gravity) waves. On the other hand, shallow cumulus clouds are themselves part of the turbulent field and, as a consequence, they modify the characteristics of the boundary layer. Therefore, studying the life cycle of shallow marine cumulus clouds enhances the understanding of the impact they have on the state of and processes within the atmosphere.

Satellite observations of the highest spatial resolution of clouds and their interactions with aerosol particles (Boucher et al., 2013) are currently performed with polar-orbiting instruments (e.g., Chepfer et al., 2010; Delanoë & Hogan, 2010; Mace et al., 2009; Naud et al., 2010). These observations, however, only provide snapshots of the clouds at a single time throughout their evolution and are insufficient to assess potential effects on the cloud life cycle (Quaas et al., 2020).

Observations with instruments on geostationary satellites provide time-resolved measurements of the same region, though at the expense of less spatial and spectral detail compared to data from polar-orbiting sensors. Geostationary observations enable the tracking of individual clouds and cloud systems over time (Endlich & Wolf, 1981; Menzel, 2001). These tracking methodologies can be used to improve the forecast of severe weather (Vila et al., 2008), study and characterize the development of severe convective storms (Senf & Deneke, 2017; Senf et al., 2015) or warm convective cloud fields (Bley et al., 2016), or gain insight into the glaciation of convective clouds (Coopman et al., 2019, 2020). However, tracking of clouds for investigating specific scientific questions under a wide range of conditions has not yet been fully automated. Hence, considerable manual effort was spent in past studies to identify cases suitable to address a specific question.

Generally, tracking methods are based on object identification. The computation and treatment of centers of gravity or extreme values within an area that exceeds a certain threshold value, e.g., brightness temperature, RADAR reflectivity, or lightning density, is often used (Carvalho & Jones, 2001; Coopman et al., 2019; Schiesser et al., 1995; Schröder et al., 2009; Steinacker et al., 2000; Vila et al., 2008). Then, observations of a cloud or convective system in two temporally consecutive images are linked by (a) manual trajectory construction (Senf et al., 2015), (b) maximum overlap (Coopman et al., 2019; Schröder et al., 2009; Vila et al., 2008; Williams & Houze, 1987), or (c) by spatial cross-correlation (Bley et al., 2016; Carvalho & Jones, 2001; Heikenfeld et al., 2019). For a better exploitation of the vast data sets produced by geostationary sensors or numerical models, the often involved manual work has to be replaced with objective methods such as the Tracking and Object-Based Analysis of Clouds (tobac, Heikenfeld et al., 2019) algorithm.

Flow visualization is important in experimental fluid mechanics. For instance, the spatially distributed velocity field in transparent fluids can be obtained by means of Particle Image Velocimetry (PIV, Adrian, 2005; Adrian & Westerweel, 2010; Raffel et al., 2007). PIV is a particle-based contact-free optical measurement technique that employs particle tracers, laser light, and a camera to gain quantitative information regarding flow characteristics in a fluid (Seelig et al., 2018, 2019). The recorded images of scattered laser light are separated by a known time step. Two temporally consecutive images are cross-correlated to extract the displacement within the given time interval. Here, this methodology is applied to infer the displacement of clouds detected by Spinning Enhanced Visible and InfraRed Imager aboard Meteosat Second Generation (MSG-SEVIRI), to compile tracks of those clouds, and to study their physic-property temporal evolution along the track throughout their life time. Note that meteorological parameters are vital for understanding the evolution of cloud properties. Future studies that make use of the product presented here should put special emphasis on properly constraining the meteorological parameters in the analysis.

The article is organized as follows. Section 2 provides detailed technical information about the used data, the retrieval methodology, and the tracking algorithm. Section 3 presents results regarding cloud life time, cloud extent, the life cycle with respect to physical properties for clouds in different temporal regimes, and the contribution of clouds in different size regimes regarding the daily cloud reflectance. A summary of the results and conclusions are provided in Section 4.

2. Data and Methodology

2.1. MSG-SEVIRI and the CLAAS-2 Data Set

The Spinning Enhanced Visible and InfraRed Imager (SEVIRI, Schmetz et al., 2002) is the main instrument on the European geostationary Meteosat Second Generation (MSG) satellites. The SEVIRI radiometer

operates on 12 spectral channels and images the Earth from 36,000 km height above the intersection of equator and the Greenwich meridian with a temporal resolution of 15 min. Eight measurement channels cover bands in the thermal infrared and provide temperature information related to clouds, land, and the sea surface. The remaining four channels are in the visible. All channels feature a horizontal resolution of 3×3 km^2 at nadir except for the more detailed 1×1 km^2 at nadir of the high-resolution visible channel. A full image of the SEVIRI instrument covers Europe, Africa, the Middle East, and the Atlantic Ocean.

SEVIRI measurements are used to infer the properties of clouds. The thus derived Satellite Application Facility on Climate Monitoring (CM SAF, Schulz et al., 2009) CLoud property dAtAset using SEVIRI - Edition 2 (CLAAS-2, Benas et al., 2017) is an upgraded version of CLAAS (Stengel et al., 2014) and covers the time period from 2004 to 2017 (Finkensieper et al., 2020). CLAAS-2 provides information on cloud micro- and macro-physical parameters. Fractional cloud coverage is described by the cloud mask which features six categories: cloud free, cloud contaminated, cloud-filled, undefined, snow/ice at the surface (under cloud-free conditions), and non-processed. The retrieved cloud physical properties (CPP) include cloud type and thermodynamic phase, cloud top pressure, cloud top height (CTH), cloud top temperature (CTT), cloud optical thickness (COT), liquid and ice cloud water path (CWP), and cloud droplet effective radius at cloud top (CDER). All cloud products are available at native SEVIRI grid (3×3 km^2) and repeat cycle (level 2) and as daily and monthly averages and histograms (level 3).

The SEVIRI channels in the visible have undergone intercalibration between the SEVIRI instruments on MSG-1, MSG-2, and MSG-3 as well as with the Moderate Resolution Imaging Spectrometer (MODIS) on Aqua (Meirink et al., 2013). The CLAAS-2 cloud products were validated against independent reference data sets such as observations of total cloud cover made at meteorological surface stations (i.e., synoptic observations), MODIS collection 6, data from microwave sounders, and observations with spaceborne lidar and radar instruments as the Cloud-Aerosol Lidar with Orthogonal Polarization (CALIOP) aboard the Cloud-Aerosol Lidar and Infrared Pathfinder Satellite Observation satellite, and the Cloud Profiling Radar onboard CloudSat (Benas et al., 2017; Finkensieper et al., 2016; Li et al., 2000; Stephens et al., 2002; Winker et al., 2007). CLAAS-2 cloud detection was carefully validated against CALIOP and reveals a probability of detection score of 87.5% (Benas et al., 2017). The corresponding false alarm ratio is 16.9% and the hit rate reaches 80.9%. Differences between day and night are minor (2.2%) and the cloud probability of detection is significantly higher over sea than over land (17.9%) at the cost of a much higher false alarm ratio. Note, CLAAS-2 detects only approximately 50% of the CALIOP cloud type "low broken cumulus", which according to CALIOP, occurs by about two orders of magnitudes less often than "cirrus". The accuracy of cloud top products was also analyzed and reveals Pearson correlation coefficients of greater than 0.84 for comparisons with CALIOP for all cloud top products. Validation against MODIS reveals a small bias in CTH for low clouds and a very good agreement for COT between the two products. Furthermore, the CLAAS-2 CDER for liquid clouds agrees well with the MODIS 1.6 μm CDER and the CWP is proportional to the product of COT and CDER and, thus, shows their combined features, resulting in very good agreement for liquid clouds (Benas et al., 2017; Finkensieper et al., 2016). In summary (and besides less detection of "low broken cumulus" clouds), the validation efforts found no major discrepancies in spatial distribution and temporal variability of the inferred products apart from small deviations that can be attributed to differences in sensor characteristics, retrieval approaches, spatial and temporal sampling, and viewing geometry. The fractional cloud coverage product in the CLAAS-2 data record is an ideal starting point for the identification and tracking of individual clouds—particularly as CPP of a tracked cloud can be conveniently extracted from the same data set at once.

In this study, we have tracked clouds and characterized their temporal evolution using CLAAS-2 level 2 products in the region around the Canary Islands during August 2015. Figure 1 gives an overview of this region and shows an example of the trajectories of tracked clouds.

2.2. Cloud Identification and Tracking

The cloud tracking methodology consists of four steps: (a) import data from two consecutive time steps, (b) identification of clouds in the cloud mask, (c) calculation of cloud velocity, and (d) link identified clouds in

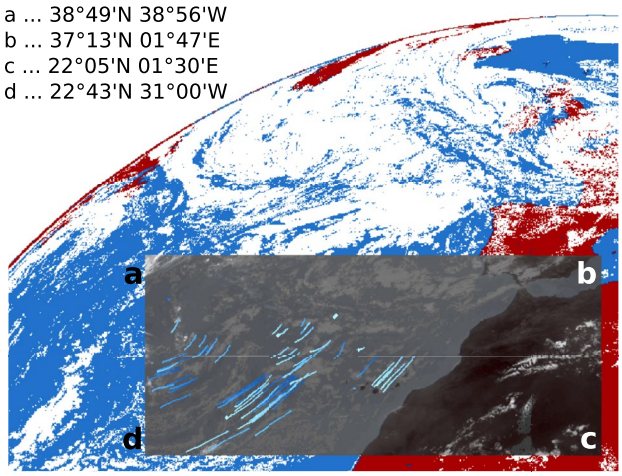

Figure 1. Composite of the land-sea mask and the CLAAS-2 cloud mask at 13:00 UTC on August 24, 2015 with pixels referring to land (dark red), sea (blue), and cloudy conditions (white). The inset in grayish colors shows the region considered in this study. The blue lines in the inset mark about 100 cloud trajectories with life times ≥7 h identified in the time period from 00:00 UTC on August 23, 2015 to 23:45 UTC on August 24, 2015. Darker blue marks older trajectories. Light blue blobs at one end of some trajectories visualize the area covered by the cloud at the latest time step and point to further cloud development.

consecutive time steps. These four steps are repeated for the considered time series. The code has been parallelized to optimize computational performance.

The CLAAS-2 cloud mask is used to identify clouds, construct their trajectories, and infer time series of their physical properties together with their life time. For the moment, there is no distinction made between cloud types, and the data set can still be contaminated by multilayered clouds. The information in the cloud mask is used to construct a binary 2d image by setting fully cloudy pixels to unity and all other pixels to zero. To uniquely identify single fully cloudy pixels and/or clouds composed of several cloudy pixels (connected components), the next step assesses pixel connectivity. Either single cloudy pixels or cloudy pixels that have a cloudy neighbor along each of their edges are identified as connected components (Haralick & Shapiro, 1992). Those are uniquely labeled with integer values greater than or equal to zero in which pixels labeled zero are the background, pixels labeled one make up the first cloud, pixels labeled two make up a second cloud, and so on.

After the images with the clouds that should be tracked have been produced from the CLAAS-2 cloud mask, the PIV methodology is used to calculate the displacement of identified clouds (Sveen & Cowen, 2004). According to our knowledge, this is the first time that this technique is applied in the field of atmospheric science. A pair of binary 2d images separated by a time step of 15 min is therefore considered. Both images are divided into smaller overlapping sub-windows of size $M \times N$. Hereafter, $I_1^{i,j}$ denotes sub-window (i, j) in the image of the initial time step and $I_2^{i,j}$ the corresponding sub-window (i, j) in the image of the subsequent time step. The evaluation of the displacement field is based on cross-correlation and calculated as:

$$R(s,t) = \sum_{m=1}^{M} \sum_{n=1}^{N} I_1^{i,j}(m,n) \cdot I_2^{i,j}(m-s, n-t). \quad (1)$$

Here, $R(s, t)$ is the cyclic cross-correlation, (m, n) marks the pixel locations in sub-windows $I_{1,2}^{i,j}$, and (s, t) is the 2d cyclic displacement at which the cross-correlation is computed. While Equation 1 is the standard statistical method to analyze the sub-windows of two separate images, it is quite time consuming. Therefore, Willert and Gharib (1991) suggest to apply the correlation theorem and the use of fast Fourier and inverse Fourier transforms significantly accelerates the calculation. Visually, the cross-correlation of a sub-window pair gives a correlation plane spanned by the displacements s, t. It contains a maximum at the location (s, t) for which the pattern in the two images matches best.

Velocities are analyzed with a parallelized version of MatPIV (Sveen, 2004) starting in the first pass with a sub-window size of 128 × 128 pixels. Adjacent sub-windows overlap by 50%. Originating from sub-windows that contain insufficient particle-image pairs, spurious vectors/neighbors (also called "outliers") appear. Those vectors deviate unphysically in direction and magnitude from nearby "valid" vectors (Westerweel, 1994). To detect and remove those vectors, several filters are applied in the post-processing of the intermediate displacement distribution (Sveen & Cowen, 2004):

1. A global histogram operator removes velocity vectors that are significantly larger or smaller than the derived mean velocity. The acceptance region $\mathbf{v}_{\text{min, max}}$ is calculated by plus/minus three times the standard deviation of the derived mean velocity
2. A local filter removes velocity vectors that deviate by three times the standard deviation from the median of their surrounding neighbors
3. An additional function interpolates empty pixels (NaN values) in the vector field by sorting all spurious vectors according to their number of spurious neighbors, starting the interpolation with the vector that touches the least spurious neighbors, and iterating until all empty values are filled

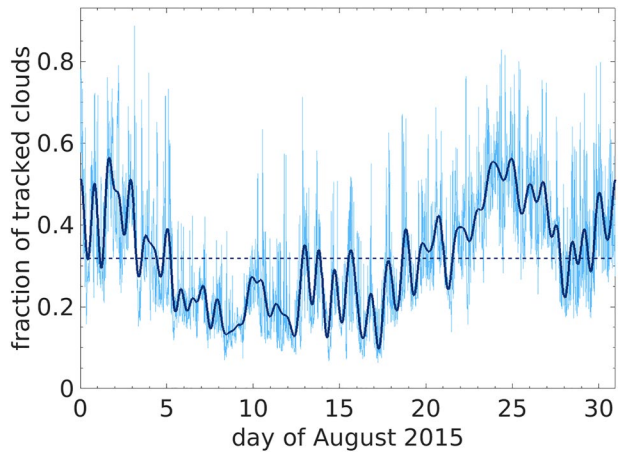

Figure 2. Development of the ratio of the area covered by a total of 2,725,620 tracked clouds related to the area covered by all cloudy pixels in the considered domain (see Figure 1) during August 2015 (light blue line). The one-day FFT-filtered fraction is given as dark blue line. The dotted line gives the mean fraction of tracked clouds of 32%.

A multi-pass approach, decreasing the sub-window size to 64 × 64, 32 × 32, and 16 × 16 pixels, permits to increase the dynamic velocity range which is defined as the ratio of the maximum measurable velocity to the minimum resolvable velocity. Especially in image recordings with high image density and a high dynamic range in the displacements, single pass correlation schemes cannot use small sub-windows without losing the correlation signal due to the larger displacements (Raffel et al., 2007). However, the vectors obtained from the first pass serve as a reference in the next pass with the next smaller sub-window (Adrian, 1997). This improves the spatial resolution and achieves displacements to subpixel accuracy. The derived displacements are linear in time and, thus, represent a mean value over the chosen time interval Δt and sub-window size. Furthermore, the displacements are connected to the center of the sub-windows. Finally, the gridded velocities are interpolated onto the positions of the centers of mass of the tracked clouds using 2d linear interpolation.

In the next step, the inferred information is used to link clouds in consecutive time steps to compile their trajectories. Knowledge of the center of mass $\mathbf{x}^k = (x_c, y_c)^k_{t_0}$ of the kth cloud and its estimated velocity $\mathbf{v}^k = (u_c, v_c)^k_{t_0}$ at time step t_0 allows for the calculation of its virtual location $\mathbf{x}^k_v = (x^v_c, y^v_c)^k_{t_0+\Delta t}$ in the consecutive image at the time $t_0 + \Delta t$ as:

$$\mathbf{x}^k_v = \mathbf{x}^k + \Delta t \mathbf{v}^k. \tag{2}$$

From the jth virtual and kth true location of the identified clouds, the distance matrix $\mathbf{D} \in \mathbb{R}^{K \times J}$, $k = 1, ..., K$; $j = 1, \ldots, J$; $K, J \in \mathbb{N}^*$ which contains the Euclidean norms $\|\mathbf{x}^j_v - \mathbf{x}^k\|$ is calculated. Here, j refers to identified clouds in the CLAAS-2 cloud mask at time step t_0 and k to identified clouds at time step $t_0 + \Delta t$. Two clouds captured in consecutive cloud mask images are considered identical, if the kth Euclidean norm related to the minimum in the jth column $\|\mathbf{x}^j_v - \mathbf{x}^k\| \leq \varepsilon$ with $\varepsilon = 2$ pixel. Or in other words, two clouds (one in each image) are declared to be the same cloud if the distance between their centers of mass is not larger than two pixels. In that case, the kth cloud identifier is harmonized with the jth cloud identifier.

2.3. Restrictions and Inferred Parameters

The matching approach outlined above is appropriate for situations in which the distance to adjacent clouds (considering their centroids) is large enough to not interfere with the assignment of clouds at different time steps (Adrian & Westerweel, 2010). A problem occurs when clouds grow and merge with neighboring clouds or a cloud complex splits up into smaller clouds. In that case, a trajectory simply ends as the current methodology does not consider splitting and merging of clouds.

The output of the tracking algorithm is tracks of the geographical location of the identified clouds together with their life time t_c and length of the cloud track from formation to dissolution. Figure 2 presents the success rate of the tracking methodology in the form of the ratio of the area covered by a total of 2,725,620 tracked clouds related to the area covered by all cloudy pixels in the considered domain (see Figure 1) during August 2015. Very short-lived clouds, whose occurrence rate depends on the time of day and the prevailing weather conditions, contribute considerable variability to the fraction of tracked clouds. The largest fraction of tracked clouds is found for the periods around August 2 and 24. On those days, the large-scale condition allowed for the development of scattered cumulus clouds. In more detail, at the northeastern/eastern edge of the Azores high, stably stratified fresh air is advected in the domain with wind from north to northeast. Convective clouds grow vertically and may hit an existing inversion. Then, they grow horizontally and may merge with neighboring clouds, causing the trajectory to end. In subsequent time steps, the larger clouds are reliably identified by the algorithm but due to the spatial variability of the centroid, they are not connected or only connected in two or a few consecutive time steps which in turn yields peaks in Figure 2. Other times are influenced by the passage of cold and warm fronts where stratified clouds dominate. As described before, the methodology identifies such large cloud fields but does not connect the centroid, or does so in just two or a few consecutive time steps. These large cloud complexes often split up into many small

clouds which in turn can be tracked with high accuracy. Consequently, the results presented in this article are restricted to relatively isolated clouds. Considering the overlap of cloudy objects as in Lakshmanan and Smith (2010), Schröder et al. (2009), or Coopman et al. (2019) will improve the algorithm in future versions. The low-pass filtered fraction of tracked clouds in Figure 2 shows variability on diurnal and weekly scale that varies around a mean fraction of tracked clouds of approximately 32%.

Geometrical properties of the tracked clouds are derived from the cloud mask for each time step. This includes the centroid (center of mass) of the cloud and the cloud pixel positions. Cloud extent A_c for each time step is derived from auxiliary data in the CLAAS-2 data set that provides the surface area covered by each pixel derived from a spherical approximation of the earth.

Knowledge of the pixel positions of the clouds along their tracks allows to furthermore extract pixel-wise information regarding their physical properties from the CLAAS-2 data set. These include cloud phase, COT, CWP, cloud droplet number concentration (CDNC) calculated following Equation 6 in Quaas et al. (2020), CDER, CTH, and CTT.

2.4. Filtering and Analysis of Identified Cloud Tracks

The methodology reliably tracks relatively isolated clouds. Formation and life cycle of these clouds may be different regarding the underlying surface (sea or land), the presence of different aerosol types, or the altitude level. To reduce the impact of these effects, the study focuses on shallow marine cumulus clouds over a specific area. Several techniques can be used to filter the identified clouds.

1. **Cloud location:** Considering one track, each cloud pixel of the first and last time step is checked for being over land, coast, or sea. If any pixel is over land or coast the track is excluded
2. **Cloud environment:** To extract well-defined tracks, each cloud pixel of the first/last time step is checked to be cloud free with respect to the previous/subsequent time step to filter for clouds that form and dissolve in clear air
3. **Cloud top height:** The CTH is considered for identifying shallow cumulus clouds. Genkova et al. (2007), Mieslinger et al. (2019), and Zhao and Di Girolamo (2007) derived CTH values from high-resolution Advanced Spaceborne Thermal Emission and Reflection Radiometer (ASTER) imagery. Genkova et al. (2007) found a bimodal frequency distribution with a primary peak at 0.65 km, while Zhao and Di Girolamo (2007) found it at 0.9 km and a much smaller secondary peak at 1.5 km. Mieslinger et al. (2019) found scene-averaged CTH values well below 3 km and a broad peak at height levels between 0.8 and 1.2 km well below their average value of 1.3 km. The latter authors argue, the differences between studies might be due to retrieval errors in the different CTH calculations. But, they may also originate from different weather conditions in distinct study regions. All studies discuss factors for CTH-uncertainty. A high-bias of about 0.2 km due to possible water vapor absorption was reported by Zhao and Di Girolamo (2007). Genkova et al. (2007) found a low height bias of about 0.25 km in the ASTER infrared window retrieval compared to the more accurate stereo height retrieval. In broken low-level cloud scenes with cloud coverage of about 20%–30% a 0.45 km bias was found by Greenwald et al. (2018) between MODIS 6 Collection CTHs and CALIOP layer top height when an inversion is present while without inversion the bias is about 0.42 km. The bias is mainly attributed to the influence of the warm ocean surface on 1 km MODIS brightness temperatures in partly cloudy pixels. Considering the limitations, those trajectories were selected that have (pixel-wise) minimum CTH(t) larger or equal to 0.45 km and its maximum CTH(t) not exceeds 3.5 km. Figure 3 shows the vertical bimodal distribution of spatial-median CTHs found during day and nighttime. A primary peak is found at 1.36 km slightly above the distribution average $\mu = 1.16$ km, and a smaller secondary peak appears at height level 0.77 km. At height level 1.66 km a much smaller third peak is observed
4. **Cloud extent:** The data set is further sub-sampled to clouds with a cloud extent at any time of the life cycle $A_c(t)$ lower than 15,000 km^2. It includes a total of 250,146 shallow marine cumulus clouds that existed at day and nighttime. Taking the probability of CLAAS-2 low-level cloud detection into account, it is not surprising that the data set reduces by one order of magnitude
5. **Cloud properties:** The CPPs are available only during daytime as their retrieval requires information from MSG-SEVIRI's solar channels (Stengel et al., 2014). Also, taking higher uncertainties in cloud detection for optically very thin clouds into account, the data set was further sub-sampled for clouds with a

Table 1
Number of Cloud Tracks Identified in the Study Region in August 2015 for the Different Filtering Described in Section 2.4

Cloud filter	Tracks
All	2,725,620
Marine clouds with 0.45 km ≤ CTH(t) < 3.5 km and $A_c(t)$ < 15,000 km^2, and clear air	
Day and nighttime	250,146
Daytime and min(COT(t)) ≥ 0.3	31,748
Daytime, min(COT(t)) ≥ 0.3 and t_c ≥ 0.5 h	11,422
t_c ≤ 1 h	9,893
t_c > 1 h	1,529

spatially (pixel-wise) minimum COT greater than or equal to 0.3. This gives a total of 31,748 clouds that existed entirely during daytime, i.e., for which CPP data is available throughout their full life time. The spatial-median CTH distribution considering the daytime set in Figure 3 shows no significant differences compared to the day and nighttime set except the number of observations is about one order smaller, which in addition can also be attributed to numerous merging events that reduce the daytime set

The CLAAS-2 CPPs are analyzed along the cloud tracks to infer the spatial median, spatial extrema, and changes throughout cloud life time. A relative time axis is introduced that respectively scales t_c between [0, 1] and interpolates the CPPs at the specific query points. An overview of the number of cloud tracks identified for the different scenarios considered in the analysis is given in Table 1.

Furthermore, distributions of the content of liquid cloud water (LCW) as a function of (a) cloud life time t_c, and (b) cloud extent A_c (cf. Figures 4a and 4b) are derived. Initially, the time series of LCW is constructed summing up the product of pixel-wise CWP and surface area covered by each pixel for each time step. In case of the first distribution, time series are filtered for tracks that fulfill the two criteria listed in the lower part of Table 1. The distinct sets of LCW time series are re-arranged into two arrays. Then, these values are sorted into logarithmically equally sized bins to calculate the probability density functions (PDFs). In case of the second distribution, an array that contains the full set of LCW time series was produced keeping the information on cloud extent. Based on the findings in Figure 4b, values of cloud water are sorted into five subsets concerning cloud areal extent. Four subsets in the range of the scaling parameter α_1 were chosen and one subset for the range of scaling parameter α_2, whereas α_1 and α_2 will be described in Section 3.1. These are respectively (a) A_c < 21 km^2, (b) 21 ≤ A_c (km^2) < 42, (c) 42 ≤ A_c (km^2) < 84, (d) 84 ≤ A_c (km^2) < 170, and (e) A_c ≥ 170 km^2. Values of each set were again sorted into logarithmically equally sized bins to calculate the PDFs.

3. Results

3.1. Cloud Life Time and Cloud Extent

This section presents the findings in the form of PDFs. For those tracks of shallow marine cumulus that existed at day and nighttime values of t_c are sorted into equally sized 0.25 h bins to calculate the PDF. Figure 4a shows the distribution in double-logarithmic scale. Two regimes with different characteristic scaling can be identified, although a robust scale brake is not observed. Nevertheless, a double power law fit with exponents $\alpha_1 \approx -5/3$ and $\alpha_2 \approx -4$ for shorter and longer cloud life times, respectively is found. The first scaling might be attributed either to isotropic turbulence in the inertial subrange (Kolmogorov, 1941) or to mesoscale processes which operate on horizontal scales from approximately 1 km to several hundreds of kilometers (Nastrom et al., 1984). The second scaling might be due to synoptic-scale motions. The first comprehensive atmospheric kinetic energy spectra derived from measurement of the zonal and meridional wind components near the tropopause level by commercial aircraft was provided by Nastrom et al. (1984). They identified two dynamic regimes with power-law dependencies upon wavenumber following a −3 scaling in the synoptic-scale range (for wavelengths between 500 and 3,000 km), and a −5/3 scaling in the mesoscale range. The observed −3 power dependence on wavenumber is considered evidence of an

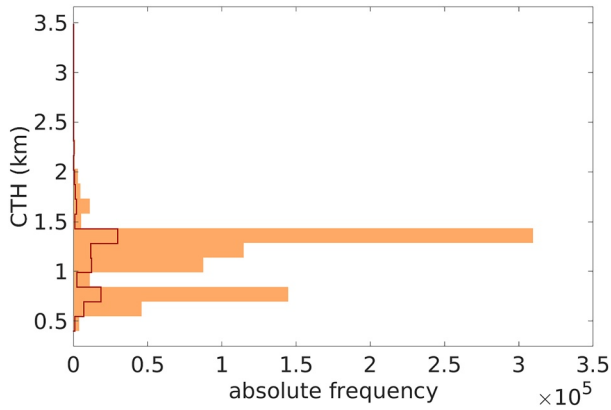

Figure 3. The vertical distribution of spatial-median cloud top heights found respectively during (a) day and nighttime (orange) and (b) daytime (red line). The distribution average is $\mu = 1.16$ km.

enstrophy cascade from low to high wavenumbers and Charney's theory described the process as geostrophic turbulence (Charney, 1971). Our finding of the steeper −4 power law scaling might be due to considering just shallow marine cumulus clouds and the limited spatial resolution of the SEVIRI observations.

The cloud extent PDF (Figure 4b) was derived by sorting values of $A_c(t)$ into logarithmically equally sized bins. A double power law is observed with a scaling parameter of $\alpha_1 = -1.62$ for clouds up to 170 km^2 in size and a scaling parameter of $\alpha_2 = -3.34$ for larger clouds. Mieslinger et al. (2019) found a double power law for which the scale breaking cloud area at 0.27 km^2 is far smaller than the native SEVIRI resolution. Beyond the scale break up to about 1,000 km^2 they found a scaling parameter of −1.06. Koren et al. (2008) studied observational data and reported a scaling parameter of −1.3, while Peters et al. (2009) found a scaling parameter of −2.06 from using different observational data, percolation theory, and linear binning. Mieslinger et al. (2019) provide the mathematical relation between the scaling parameters derived from different binning methods. Applying the change-of-variable technique to the scaling parameter found by Peters et al. (2009) yields −1.06. Taking into account the much larger domain and the coarser resolution of the SEVIRI data, our finding is in good agreement with the reported earlier findings. However, the focus on tracks of relatively isolated cumulus clouds leads to a difference in the scaling especially for clouds with larger spatial extent.

3.2. Cloud Physical Properties

The analysis presented in this section considers the 11,422 cloud tracks that fulfill the criteria listed in the lower part of Table 1. Those clouds existed only during daytime, formed and dissolved in clear air, and have temporal connections for at least three time steps. The latter condition was applied to ensure minimal sampling. The daytime set was further subdivided into two categories of life times (a) smaller than or equal to or (b) larger than one hour (see also the two lowermost conditions in Table 1) and relative time series of median and interquartile CPPs were calculated. The median CTT (not shown) for the two sets varies between 292 and 294 K. It is approximately constant throughout cloud development, as the investigation is focused on liquid clouds. On average, CTT is about 2 K higher for clouds that exceed life times of one hour compared to clouds that exist for a shorter time period. The temporal evolution of CTH (not shown) reveals that short-lived clouds show a larger median CTH that is increased by about 90 m.

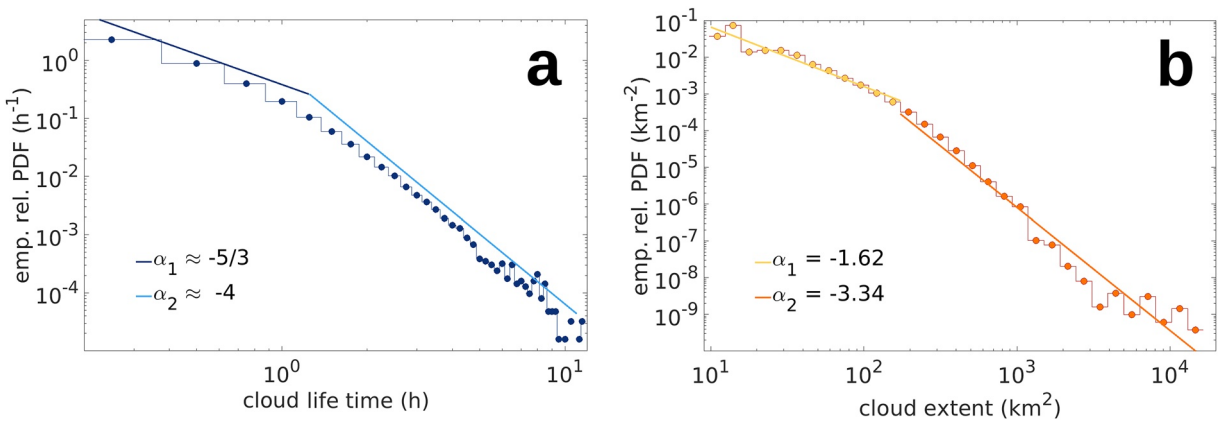

Figure 4. Probability density function of (a) cloud life time and (b) cloud extent for 250,146 tracked shallow marine cumulus clouds that formed and dissolved in clear air during day and nighttime.

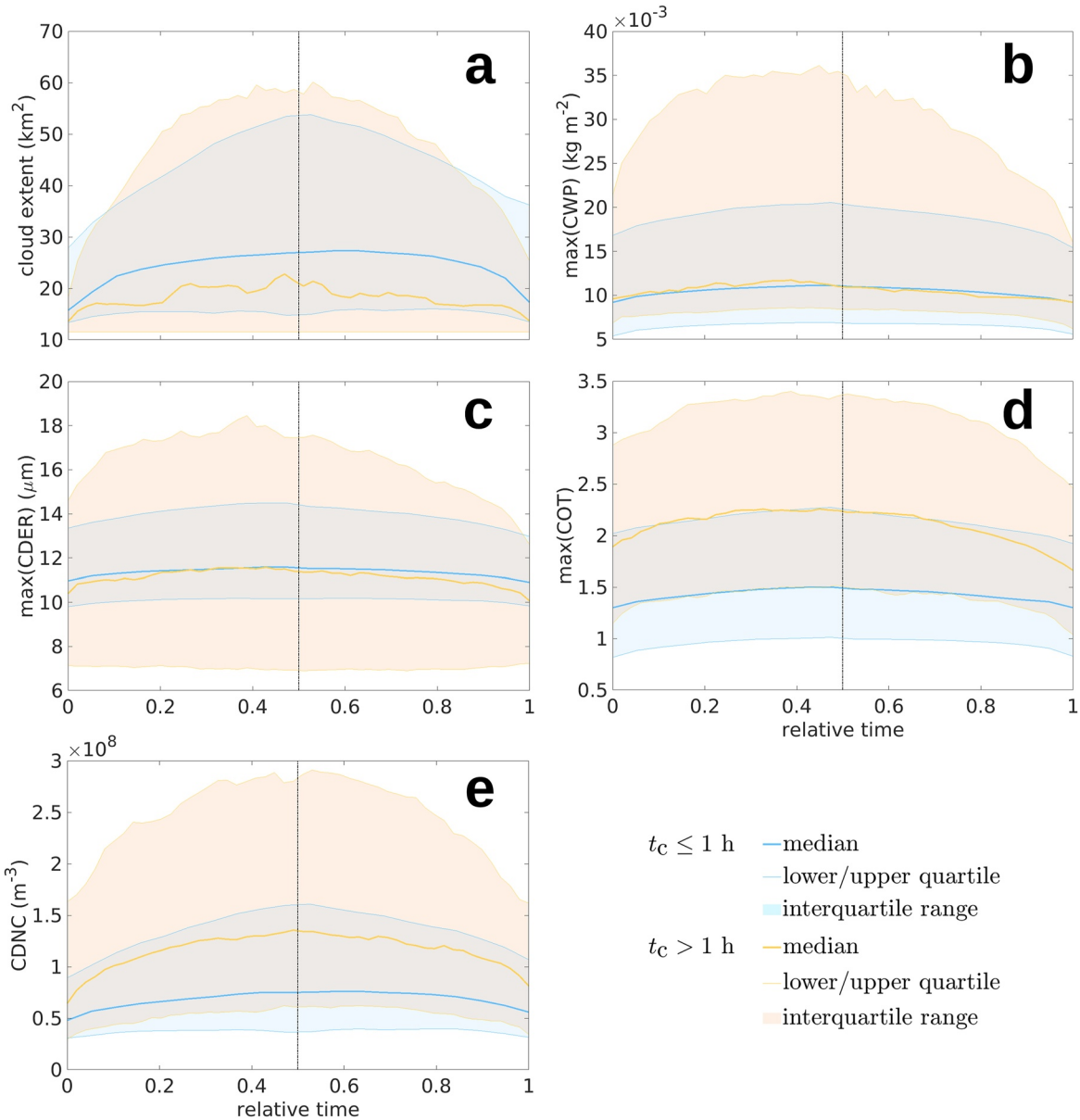

Figure 5. Evolution of median values (bold lines) and interquartile range (colored areas) of physical properties of the shallow marine cumulus clouds fulfilling the lowermost three conditions in Table 1 as a function of relative time scaled between [0, 1]: (a) cloud extent, (b) maximum cloud water path, (c) maximum cloud droplet effective radius, (d) maximum cloud optical thickness, and (e) cloud droplet number concentration. Blue relates to cloud life times lower than or equal to one hour while orange marks cloud life times that exceed one hour.

The discussion begins with the evolution of cloud extent A_c (Figure 5a). For the two scenarios, the median A_c about doubles until the middle of the cloud's life time. Decreasing cloud extent characterizes the second part of the cloud's life time. The curve for clouds that exist for longer than one hour shows more variability as a result of higher sampling. Median values are consistently larger for short-lived clouds, while the interquartile range for long-lived clouds exceeds the values of short-lived clouds except at the beginning/end of the time period. Growth until the mid of life time and decrease for the second half also characterizes the evolution of the other investigated CPP independent of the considered scenario. The evolution of median values of maximum CWP and maximum CDER (Figures 5b and 5c) is identical for short- and long-lived clouds and reaches values of 11 kg m^{-2} and 11.5 μm, respectively. Notable is a larger interquartile range for clouds that exist for longer than one hour and show the highest values in the first part of their life time. The evolution of median values of maximum COT (Figure 5d) differs for the considered scenarios. Short-lived

clouds have median values of maximum COT of about 1.5 showing an interquartile range of ±0.5. The long-lived clouds reach median values of about 2 and a lower quartile of 1.5 while the upper quartile is about 3.5. Although we focus on presenting maximum values of COT, the investigated clouds seem optically thin. COT values of pixels fulfilling the marine, daytime, CTH, and minimum COT criteria (cf. Section 2.4) lead to a median of 3.41, a lower quartile of 1.64, and an upper quartile of 6.81. These values support the finding listed before although they are slightly higher due to optically thick pixels in synoptic-scale cloud complexes that are excluded from tracking. Although CWP and CDER show equal values for the considered scenarios, the droplet number concentration (Figure 5e) is about a factor of two higher due to partly denser clouds that have life times larger than one hour compared to the short-lived clouds. An optically denser cloud that has a slightly lower CTH and cloud extent, as well as a higher droplet number concentration, seems to be closer to the assumption that a cloud is a drifting imperishable tropospheric phenomenon and in summary these properties suggesting to be the key elements for longer cloud life time. Although the statistics show that smaller clouds have longer life times, it does on the other hand not necessarily mean that it is the small size that helps clouds to live longer. For example, it seems possible that dynamic factors (not directly observed by SEVIRI) would make clouds of both small size and long life time. Alternatively, the inverse relationship between cloud size and life time might come from the used data selection method, namely from the exclusion of clouds that split apart or merge with other clouds. While a short life time may not allow for many mergers and split-ups, their likelihood among long-living clouds may be higher for large clouds than for small clouds. This may result in the exclusion of many large clouds and may bias the remaining long life time cloud population toward smaller sizes. In nature, a cloud is the product of a multitude of complex physical feedback processes. The cloud evolves if cloud-forming processes predominate and begins to dissolve when regressive processes gain the upper hand. Cloud-forming processes are condensation of supersaturated water vapor on suitable aerosol particles or deposition of water vapor as ice on freezing nuclei. Condensation is the main process, which already occurs at a supersaturation of water vapor of a maximum of 1% on cloud condensation nuclei. Supersaturation of water vapor on the other hand is caused by (a) an increase of water vapor by evaporation, (b) cooling below the dew or frost point, (c) through adiabatic cooling, or a combination of these processes. The majority of clouds in the marine troposphere are formed by adiabatic cooling. Processes leading to adiabatic cooling are (a) turbulence in the planetary boundary layer, (b) large-scale uplift processes, i.e., at warm fronts, (c) atmospheric waves (waves at inversions or wind shear layers), and (d) convection. To estimate the CDNC cloud adiabaticity is assumed. Passive satellite observations lack the information of cloud adiabaticity within a sufficient uncertainty range and the consideration of an independent method to estimate homogeneous as well as inhomogeneous mixing processes would be highly desirable (Merk et al., 2016).

The distribution of the content of LCW controls the cloud radiation effect. Chen et al. (2000) studied radiative effects of cloud-type variations using satellite data and a radiative transfer model. The authors report a global annual mean radiative cooling effect of cumulus clouds at the top of atmosphere of $-4.6\ \mathrm{W\,m^{-2}}$. More recently, Hirsch et al. (2015) analyzed the contribution of small convective clouds to the reflectance of the total cloud field during eastern Mediterranean summer. The study found that clouds with thickness of tens to hundreds of meters contribute from approximately 35% up to 80% of the daily cloud reflectance, while imposing an average cooling effect of -0.94 to $-3.6\ \mathrm{W\,m^{-2}}$. The authors suggest that the contribution of very small clouds to the total forcing can be significant. Figure 6a shows PDFs of LCW constrained for cloud life time t_c. Short and long-lived clouds contribute equally to the LCW of 2×10^4 kg. The following range up to 5×10^6 kg is dominated by short-lived clouds and their contribution is about one order of magnitude higher, while beyond this value the contribution of long-lived clouds to the content of LCW is pronounced. Notably is an exception at about 1×10^5 kg, where the curve for long-lived clouds approaches and even exceeds values related to short-lived clouds. The PDFs of LCW as a function of cloud extent A_c (Figure 6b) are comparable regarding shape, they show first an increase with increasing LCW reaching a maximum and decrease subsequently with moderate slope. Until reaching the PDF maximum, very small clouds contribute most and large clouds fewest to LCW. In contrast to LCW, PDFs of CWP for clouds of different size ranges (not shown) present a similar maximum occurrence rate of CWP at around 10^{-2} kg $\mathrm{m^{-2}}$ with magnitude changes according to the change in the bin width. Since the A_c is constrained twice, the maximum shift to higher LCW when increasing the cloud extent subset. Beyond the maximum, the next larger subset approaches and even slightly exceeds the values of the smaller subset to contribute to

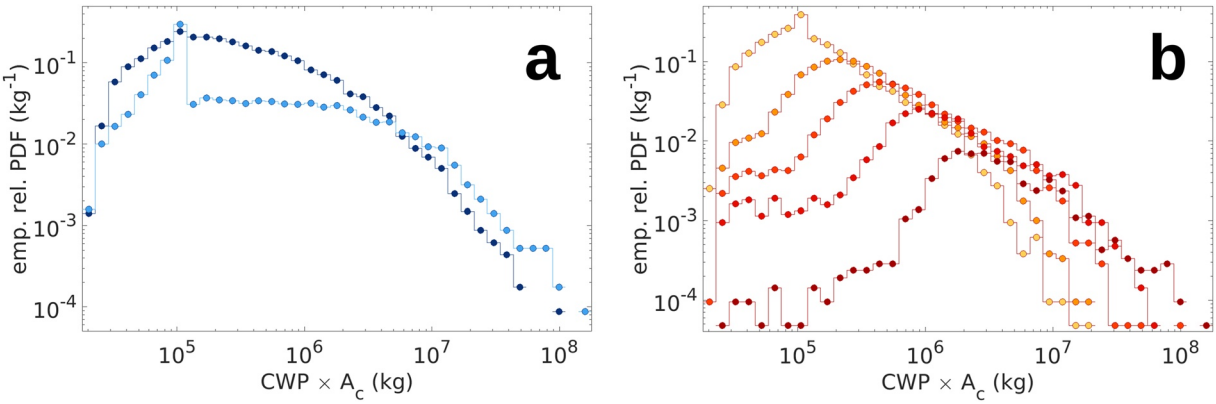

Figure 6. Probability density function of cloud water. The curves consider respectively (a) short (dark blue: $t_c \leq 1$ h) and long (light blue: $t_c > 1$ h) cloud life times, and (b) cloud extent (yellow: $A_c(\text{km}^2) < 21$; orange: $21 \leq A_c(\text{km}^2) < 42$; light red: $42 \leq A_c(\text{km}^2) < 84$; red: $84 \leq A_c(\text{km}^2) < 170$; dark red: $A_c(\text{km}^2) \geq 170$).

LCW. Although the cloud extent is far beyond those investigations given above, the present study supports the assumption and substantiates that small (in native SEVIRI resolution) and short-lived shallow marine cumulus clouds contribute significantly to daily cloud reflectance.

4. Summary and Outlook

Time-resolved measurements from instruments aboard geostationary satellites are the key for observing the temporal evolution of clouds and for quantifying the change in their physical properties throughout their life time. Furthermore, cloud tracking is also the only way to look at the temporal evolution of individual cloud properties with observations that can be compared with models. This article describes a methodology for tracking individual cumulus clouds in observations of MSG-SEVIRI and presents initial findings of its application. Specifically, the CLAAS-2 cloud mask is used to separate cloudy from cloud-free air and to identify clouds that are subsequently tracked by means of PIV. The thus derived information on the location and extent of clouds at different time steps is further used to extract cloud phase, COT, CWP, CDER, CTH, CTT, and CDNC from the CLAAS-2 package and derive median and minimum/maximum values of these properties for individual clouds throughout their life time.

The methodology is applied to CLAAS-2 data for August 2015 in a region around the Canary Islands. On average, clouds representing about 32% of the entire cloudy area in the selected domain could be tracked. A more detailed analysis was applied to tracks of shallow marine liquid clouds with top heights larger than or equal to 0.45 km and below 3.5 km, and $A_c(t) < 15{,}000$ km^2 that (a) could be followed throughout their entire life cycle, i.e., that formed and dissolved in clear air during day and nighttime, and (b) for which CPPs were available at each time step, i.e., daytime measurements for which CLAAS-2 CPP products can be inferred. Those criteria left respectively (a) 250,146 and (b) 31,748 out of a total of 2,725,620 tracked clouds for further analysis.

For selected day and nighttime clouds, the life time distribution follows a double power law with most clouds existing on a time scale of tens of minutes up to one hour. The cloud extent distribution taking into account the much larger domain, the coarser resolution of SEVIRI data, and just selecting tracks of relatively isolated cumulus clouds, is in good agreement with the literature and reveals a double power law. To study temporal cloud evolution, daytime measurements were used and the cloud life time was scaled to a relative time between zero and one. To ensure minimal sampling these clouds also had to exist for at least three time steps. The thus obtained data set of 11,422 cloud tracks were further stratified into two categories of life times (a) ≤ 1 h, or (b) larger. Relative time series of CPPs were statistically analyzed to infer time series of the median and quartiles. The A_c, CWP, CDER at cloud top, COT, and CDNC for clouds in the two temporal ranges show distinct growth and decay phases that are equally distributed with respect to the relative cloud life time. The comparison of short- and long-lived clouds shows that long-lived clouds are optically denser, have a slightly lower CTH, a smaller cloud extent, as well as a higher droplet number concentration. The analysis suggests that these are the key elements for facilitating longer shallow marine

cumulus cloud life time. Since further interpretation is possible it remains an open question for future investigation. Furthermore, the investigation of the content of LCW regarding cloud life time and cloud extent revealed that clouds with cloud extent smaller than 170 km^2 and short-lived clouds significantly contribute to the daily cloud reflectance.

In the next step of this work, the methodology will be further refined to also account for cloud splitting and merging and for overlap of cloudy objects which is currently not considered. In addition, the methodology will be applied to the full CLAAS-2 data set from 2004 to 2017 to study the temporal evolution of clouds, their properties, and their seasonal variation in different regions of the SEVIRI field of view. The algorithm presented here can be applied to different types of input data, such as a cloud mask, spectral radiances, or the output of numerical modeling. In future, the use of (a) cloud property retrievals with enhanced spatial resolution of 1 × 1 km^2 resulting from a modified retrieval scheme for the SEVIRI instrument (Deneke et al., 2021; Werner & Deneke, 2020), or (b) observations with the next generation of geostationary imagers such as the Advanced Baseline Imager aboard GOES-R (Schmit et al., 2005), the Advanced Himawari Imager aboard Himawari-8 (Letu et al., 2020), or the SEVIRI successor Flexible Combined Imager aboard Meteosat Third Generation (Durand et al., 2015) as input to the tracking algorithm will allow to study cloud development in much greater spatial detail and in the second case with temporal resolution of 1–10 min. This will extend the range of observable clouds that have been filtered from the analysis presented here. In addition, using the novel information on cloud development together with aerosol properties in the vicinity of the tracked clouds—particularly with active sensors that provide height-resolved information—provides a new way for studying aerosol cloud interactions in satellite observations.

Data Availability Statement

The CLAAS-2 data set can be found on the following link: https://doi.org/10.5676/EUM_SAF_CM/CLAAS/V002.

Acknowledgments
Torsten Seelig and Matthias Tesche acknowledge funding within the Franco-German Fellowship Programme on Climate, Energy, and Earth System Research (Make Our Planet Great Again-German Research Initiative, MOPGA-GRI, grant number 57429422) of the German Academic Exchange Service (DAAD), funded by the German Ministry of Education and Research. The authors thank EUMETSAT CM SAF for providing MSG-SEVIRI and CLAAS-2 data. Torsten Seelig, Matthias Tesche, Hartwig Deneke, and Johannes Quaas thank F. Müller for technical support and F. Senf for providing valuable comments on the study. The authors further thank the three anonymous reviewers for many helpful suggestions to improve the article. Open access funding enabled and organized by Projekt DEAL.

References

Adrian, R. J. (1997). Dynamic ranges of velocity and spatial resolution of particle image velocimetry. *Measurement Science and Technology*, *8*(12), 1393–1398. https://doi.org/10.1088/0957-0233/8/12/003

Adrian, R. J. (2005). Twenty years of particle image velocimetry. *Experiments in Fluids*, *39*(2), 159–169. https://doi.org/10.1007/s00348-005-0991-7

Adrian, R. J., & Westerweel, J. (2010). *Particle image velocimetry*. Cambridge University Press.

Benas, N., Finkensieper, S., Stengel, M., van Zadelhoff, G.-J., Hanschmann, T., Hollmann, R., & Meirink, J. F. (2017). The MSG-SEVIRI-based cloud property data record CLAAS-2. *Earth System Science Data*, *9*(2), 415–434. https://doi.org/10.5194/essd-9-415-2017

Berry, E., Mace, G. G., & Gettelman, A. (2020). Using A-Train observations to evaluate East Pacific cloud occurrence and radiative effects in the Community Atmosphere Model. *Journal of Climate*, *33*(14), 6187–6203. https://doi.org/10.1175/JCLI-D-19-0870.1

Bley, S., Deneke, H., & Senf, F. (2016). Meteosat-based characterization of the spatiotemporal evolution of warm convective cloud fields over central Europe. *Journal of Applied Meteorology and Climatology*, *55*(10), 2181–2195. https://doi.org/10.1175/JAMC-D-15-0335.1

Boucher, O., Randall, D., Artaxo, P., Bretherton, C., Feingold, G., Forster, P., & Zhang, X. Y. (2013). Clouds and aerosols. In *Climate Change 2013: The Physical Science Basis: Working Group I Contribution to the Fifth Assessment Report of the Intergovernmental Panel on Climate Change* (pp. 571–658). Cambridge University Press. https://doi.org/10.1017/CBO9781107415324.016

Carvalho, L. M. V., & Jones, C. (2001). A satellite method to identify structural properties of mesoscale convective systems based on the maximum spatial correlation tracking technique (MASCOTTE). *Journal of Applied Meteorology and Climatology*, *40*(10), 1683–1701. https://doi.org/10.1175/1520-0450(2001)040<1683:asmtis>2.0.co;2

Charney, J. G. (1971). Geostrophic turbulence. *Journal of the Atmospheric Sciences*, *28*, 1087–1095. https://doi.org/10.1175/1520-0469(1971)028<1087:gt>2.0.co;2

Chen, T., Rossow, W. B., & Zhang, Y. (2000). Radiative effects of cloud-type variations. *Journal of Climate*, *13*, 264–286. https://doi.org/10.1175/1520-0442(2000)013<0264:reoctv>2.0.co;2

Chepfer, H., Bony, S., Winker, D., Cesana, G., Dufresne, J. L., Minnis, P., et al. (2010). The GCM-oriented CALIPSO cloud product (CALIPSO-GOCCP). *Journal of Geophysical Research*, *115*(D4). https://doi.org/10.1029/2009JD012251

Chepfer, H., Bony, S., Winker, D., Chiriaco, M., Dufresne, J.-L., & Séze, G. (2008). Use of CALIPSO lidar observations to evaluate the cloudiness simulated by a climate model. *Geophysical Research Letters*, *35*(15). https://doi.org/10.1029/2008GL034207

Coopman, Q., Hoose, C., & Stengel, M. (2019). Detection of mixed-phase convective clouds by a binary phase information from the passive geostationary instrument SEVIRI. *Journal of Geophysical Research: Atmospheres*, *124*(9), 5045–5057. https://doi.org/10.1029/2018JD029772

Coopman, Q., Hoose, C., & Stengel, M. (2020). Analysis of the thermodynamic phase transition of tracked convective clouds based on geostationary satellite observations. *Journal of Geophysical Research: Atmospheres*, *125*, e2019JD032146. https://doi.org/10.1029/2019JD032146

Delanoë, J., & Hogan, R. J. (2010). Combined CloudSat-CALIPSO-MODIS retrievals of the properties of ice clouds. *Journal of Geophysical Research*, *115*(D4). https://doi.org/10.1029/2009JD012346

Deneke, H., Barrientos-Velasco, C., Bley, S., Hünerbein, A., Lenk, S., Macke, A., et al. (2021). Increasing the spatial resolution of cloud property retrievals from Meteosat SEVIRI by use of its high-resolution visible channel: Implementation and examples. *Atmospheric Measurement Techniques*, *14*, 5107–5126. https://doi.org/10.5194/amt-14-5107-2021

Durand, Y., Hallibert, P., Wilson, M., Lekouara, M., Grabarnik, S., Aminou, D., et al. (2015). The flexible combined imager onboard MTG: From design to calibration. In R. Meynart, S. P. Neeck, & H. Shimoda (Eds.), *Sensors, systems, and next-generation satellites XIX* (Vol. *9639*, pp. 1–14). SPIE. https://doi.org/10.1117/12.2196644

Eastman, R., Warren, S. G., & Hahn, C. J. (2011). Variations in cloud cover and cloud types over the ocean from surface observations, 1954–2008. *Journal of Climate*, *24*, 5914–5934. https://doi.org/10.1175/2011JCLI3972.1

Endlich, R. M., & Wolf, D. E. (1981). Automatic cloud tracking applied to GOES and METEOSAT observations. *Journal of Applied Meteorology and Climatology*, *20*(3), 309–319. https://doi.org/10.1175/1520-0450(1981)020<0309:actatg>2.0.co;2

Finkensieper, S., Hanschmann, T., Stengel, M., Benas, N., van Zadelhoff, G.-J., & Fokke Meirink, J. (2016). *Validation report SEVIRI cloud products CLAAS edition* (Vol. *2*). https://doi.org/10.5676/EUM_SAF_CM/CLAAS/V002

Finkensieper, S., Meirink, J. F., van Zadelhoff, G.-J., Hanschmann, T., Benas, N., Stengel, M., & Werscheck, M. (2020). *CLAAS-2.1: CM SAF cloud property data set using SEVIRI - edition* (Vol. *2.1*). https://doi.org/10.5676/EUM_SAF_CM/CLAAS/V002_01

Genkova, I., Seiz, G., Zuidema, P., Zhao, G., & Girolamo, L. D. (2007). Cloud top height comparisons from ASTER, MISR, and MODIS for trade wind cumuli. *Remote Sensing of Environment*, *107*(1), 211–222. (Multi-angle Imaging SpectroRadiometer (MISR) Special Issue). https://doi.org/10.1016/j.rse.2006.07.021

Grant, A. L. M., & Lock, A. P. (2004). The turbulent kinetic energy budget for shallow cumulus convection. *Quarterly Journal of the Royal Meteorological Society*, *130*(597), 401–422. https://doi.org/10.1256/qj.03.50

Greenwald, T. J., Bennartz, R., Lebsock, M., & Teixeira, J. (2018). An uncertainty data set for passive microwave satellite observations of warm cloud liquid water path. *Journal of Geophysical Research: Atmospheres*, *123*, 3668–3687. https://doi.org/10.1002/2017JD027638

Haralick, R. M., & Shapiro, L. G. (1992). *Computer and Robot Vision* (1st ed.). Addison-Wesley Longman Publishing Co., Inc.

Haynes, J. M., Jakob, C., Rossow, W. B., Tselioudis, G., & Brown, J. (2011). Major characteristics of southern ocean cloud regimes and their effects on the energy budget. *Journal of Climate*, *24*(19), 5061–5080. https://doi.org/10.1175/2011JCLI4052.1

Heikenfeld, M., Marinescu, P. J., Christensen, M., Watson-Parris, D., Senf, F., van den Heever, S. C., & Stier, P. (2019). tobac 1.2: Towards a flexible framework for tracking and analysis of clouds in diverse data sets. *Geoscientific Model Development*, *12*(11), 4551–4570. https://doi.org/10.5194/gmd-12-4551-2019

Heus, T., & Seifert, A. (2013). Automated tracking of shallow cumulus clouds in large domain, long duration large eddy simulations. *Geoscientific Model Development*, *6*(4), 1261–1273. https://doi.org/10.5194/gmd-6-1261-2013

Hirsch, E., Koren, I., Altaratz, O., & Agassi, E. (2015). On the properties and radiative effects of small convective clouds during the eastern Mediterranean summer. *Environmental Research Letters*, *10*(4), 044006. https://doi.org/10.1088/1748-9326/10/4/044006

Kolmogorov, A. N. (1941). The local structure of turbulence in incompressible viscous fluid for very large Reynolds numbers. *Doklady Akademiia Nauk SSSR*, *30*, 301–305.

Koren, I., Oreopoulos, L., Feingold, G., Remer, L. A., & Altaratz, O. (2008). How small is a small cloud? *Atmospheric Chemistry and Physics*, *8*(14), 3855–3864. https://doi.org/10.5194/acp-8-3855-2008

Lakshmanan, V., & Smith, T. (2010). An objective method of evaluating and devising storm-tracking algorithms. *Weather and Forecasting*, *25*(2), 701–709. https://doi.org/10.1175/2009WAF2222330.1

Letu, H., Yang, K., Nakajima, T. Y., Ishimoto, H., Nagao, T. M., Riedi, J., et al. (2020). High-resolution retrieval of cloud microphysical properties and surface solar radiation using Himawari-8/AHI next-generation geostationary satellite. *Remote Sensing of Environment*, *239*, 111583. https://doi.org/10.1016/j.rse.2019.111583

Li, F. K., Im, E., Durden, S. L., Girard, R., Sadowy, G., & Wu, C. (2000). Cloud Profiling Radar (CPR) for the CloudSat Mission. In . *IGARSS 2000. IEEE 2000 International Geoscience and Remote Sensing Symposium. Taking the pulse of the planet: The role of remote sensing in managing the environment. Proceedings (Cat. No.00CH37120)* (Vol. *7*, pp. 2821–2823). https://doi.org/10.1109/IGARSS.2000.860259

Mace, G. G., Zhang, Q., Vaughan, M., Marchand, R., Stephens, G., Trepte, C., & Winker, D. (2009). A description of hydrometeor layer occurrence statistics derived from the first year of merged CloudSat and CALIPSO data. *Journal of Geophysical Research*, *114*(D8). https://doi.org/10.1029/2007JD009755

Meirink, J. F., Roebeling, R. A., & Stammes, P. (2013). Inter-calibration of polar imager solar channels using SEVIRI. *Atmospheric Measurement Techniques*, *6*(9), 2495–2508. https://doi.org/10.5194/amt-6-2495-2013

Menzel, W. P. (2001). Cloud tracking with satellite imagery: From the pioneering work of Ted Fujita to the present. *Bulletin of the American Meteorological Society*, *82*, 33–47. https://doi.org/10.1175/1520-0477(2001)082<0033:ctwsif>2.3.co;2

Merk, D., Deneke, H., Pospichal, B., & Seifert, P. (2016). Investigation of the adiabatic assumption for estimating cloud micro- and macrophysical properties from satellite and ground observations. *Atmospheric Chemistry and Physics*, *16*(2), 933–952. https://doi.org/10.5194/acp-16-933-2016

Mieslinger, T., Horváth, A., Buehler, S. A., & Sakradzija, M. (2019). The dependence of shallow cumulus macrophysical properties on large-scale meteorology as observed in ASTER imagery. *Journal of Geophysical Research: Atmospheres*, *124*, 11477–11505. https://doi.org/10.1029/2019JD030768

Nastrom, G., Gage, K., & Jasperson, W. (1984). Kinetic energy spectrum of large-and mesoscale atmospheric processes. *Nature*, *310*, 36–38. https://doi.org/10.1038/310036a0

Naud, C. M., Del Genio, A. D., Bauer, M., & Kovari, W. (2010). Cloud vertical distribution across warm and cold fronts in CloudSat-CALIPSO Data and a general circulation model. *Journal of Climate*, *23*(12), 3397–3415. https://doi.org/10.1175/2010JCLI3282.1

Nuijens, L., Stevens, B., & Siebesma, A. P. (2009). The environment of precipitating shallow cumulus convection. *Journal of the Atmospheric Sciences*, *66*(7), 1962–1979. https://doi.org/10.1175/2008JAS2841.1

Peters, O., Neelin, J. D., & Nesbitt, S. W. (2009). Mesoscale convective systems and critical clusters. *Journal of the Atmospheric Sciences*, *66*(9), 2913–2924. https://doi.org/10.1175/2008JAS2761.1

Quaas, J., Arola, A., Cairns, B., Christensen, M., Deneke, H., Ekman, A. M. L., et al. (2020). Constraining the Twomey effect from satellite observations: Issues and perspectives. *Atmospheric Chemistry and Physics*, *20*(23), 15079–15099. https://doi.org/10.5194/acp-20-15079-2020

Raffel, M., Willert, C. E., Wereley, S. T., & Kompenhans, J. (2007). *Particle image velocimetry: A practical guide* (2nd ed.). Cambridge University Press. https://doi.org/10.1007/978-3-540-72308-0

Schiesser, H. H., Houze, R. A., & Huntrieser, H. (1995). The mesoscale structure of severe precipitation systems in Switzerland. *Monthly Weather Review*, *123*(7), 2070–2097. https://doi.org/10.1175/1520-0493(1995)123<2070:tmsosp>2.0.co;2

Schmetz, J., Pili, P., Tjemkes, S., Just, D., Kerkmann, J., Rota, S., & Ratier, A. (2002). An introduction to Meteosat Second Generation (MSG). *Bulletin of the American Meteorological Society*, *83*(7), 977–992. https://doi.org/10.1175/1520-0477(2002)083<0977:AITMSG>2.3.CO;2

Schmit, T. J., Gunshor, M. M., Menzel, W. P., Gurka, J. J., Li, J., & Bachmeier, A. S. (2005). Introducing the next-generation advanced baseline imager on GOES-R. *Bulletin of the American Meteorological Society*, *86*(8), 1079–1096. https://doi.org/10.1175/BAMS-86-8-1079

Schröder, M., König, M., & Schmetz, J. (2009). Deep convection observed by the Spinning Enhanced Visible and Infrared Imager on board Meteosat 8: Spatial distribution and temporal evolution over Africa in summer and winter 2006. *Journal of Geophysical Research*, *114*(D5). https://doi.org/10.1029/2008JD010653

Schulz, J., Albert, P., Behr, H.-D., Caprion, D., Deneke, H., Dewitte, S., et al. (2009). Operational climate monitoring from space: The EUMETSAT Satellite Application Facility on Climate Monitoring (CM-SAF). *Atmospheric Chemistry and Physics*, *9*(5), 1687–1709. https://doi.org/10.5194/acp-9-1687-2009

Seelig, T., Harlander, U., & Gellert, M. (2018). Experimental investigation of stratorotational instability using a thermally stratified system: Instability, waves and associated momentum flux. *Geophysical & Astrophysical Fluid Dynamics*, *112*, 239–264. https://doi.org/10.1080/03091929.2018.1488971

Seelig, T., Meyer, A., Gerstner, P., Meier, M., Jongmanns, M., Baumann, M., et al. (2019). Dielectrophoretic force-driven convection in annular geometry under Earth's gravity. *International Journal of Heat and Mass Transfer*, *139*, 386–398. https://doi.org/10.1016/j.ijheatmasstransfer.2019.04.068

Senf, F., & Deneke, H. (2017). Satellite-based characterization of convective growth and glaciation and its relationship to precipitation formation over central Europe. *Journal of Applied Meteorology and Climatology*, *56*, 1827–1845. https://doi.org/10.1175/JAMC-D-16-0293.1

Senf, F., Dietzsch, F., Hünerbein, A., & Deneke, H. (2015). Characterization of initiation and growth of selected severe convective storms over central Europe with MSG-SEVIRI. *Journal of Applied Meteorology and Climatology*, *54*(1), 207–224. https://doi.org/10.1175/JAMC-D-14-0144.1

Steinacker, R., Dorninger, M., Wölfelmaier, F., & Krennert, T. (2000). Automatic tracking of convective cells and cell complexes from lightning and radar data. *Meteorology and Atmospheric Physics*, *72*(2), 101–110. https://doi.org/10.1007/s007030050009

Stengel, M., Kniffka, A., Meirink, J. F., Lockhoff, M., Tan, J., & Hollmann, R. (2014). CLAAS: The CM SAF cloud property data set using SEVIRI. *Atmospheric Chemistry and Physics*, *14*, 4297–4311. https://doi.org/10.5194/acp-14-4297-2014

Stephens, G. L., Vane, D. G., Boain, R. J., Mace, G. G., Sassen, K., Wang, Z., et al. (2002). The cloudSat mission and the A-train: A new dimension of space-based observations of clouds and precipitation. *Bulletin of the American Meteorological Society*, *83*(12), 1771–1790. https://doi.org/10.1175/BAMS-83-12-1771

Stubenrauch, C. J., Rossow, W. B., Kinne, S., Ackerman, S., Cesana, G., Chepfer, H., et al. (2013). Assessment of global cloud data sets from satellites: Project and database initiated by the GEWEX radiation panel. *Bulletin of the American Meteorological Society*, *94*(7), 1031–1049. https://doi.org/10.1175/BAMS-D-12-00117.1

Sveen, J. K. (2004). *An introduction to MatPIV v. 1.6.1* (eprint series(2)). Dept. of Math. University of Oslo, Mechanics and Applied Mathematics.

Sveen, J. K., & Cowen, E. A. (2004). Quantitative imaging techniques and their application to wavy flows. In *PIV and water waves* (pp. 1–49). https://doi.org/10.1142/9789812796615_0001

Tselioudis, G., Rossow, W. B., Jakob, C., Remillard, J., Tropf, D., & Zhang, Y. (2021). Evaluation of clouds, radiation, and precipitation in CMIP6 models using global weather states derived from ISCCP-H cloud property data. *Journal of Climate*, *34*(17), 7311–7342. https://doi.org/10.1175/JCLI-D-21-0076.1

Vignesh, P. P., Jiang, J. H., Kishore, P., Su, H., Smay, T., Brighton, N., & Velicogna, I. (2020). Assessment of CMIP6 cloud fraction and comparison with satellite observations. *Earth and Space Science*, *7*(2), e2019EA000975. https://doi.org/10.1029/2019EA000975

Vila, D. A., Toledo Machado, L. A., Laurent, H., & Velasco, I. (2008). Forecast and tracking the evolution of cloud clusters (ForTraCC) using satellite infrared imagery: Methodology and validation. *Weather and Forecasting*, *23*(2), 233–245. https://doi.org/10.1175/2007WAF2006121.1

Werner, F., & Deneke, H. (2020). Increasing the spatial resolution of cloud property retrievals from Meteosat SEVIRI by use of its high-resolution visible channel: Evaluation of candidate approaches with MODIS observations. *Atmospheric Measurement Techniques*, *13*(3), 1089–1111. https://doi.org/10.5194/amt-13-1089-2020

Westerweel, J. (1994). Efficient detection of spurious vectors in particle image velocimetry data. *Experiments in Fluids*, *16*, 236–247. https://doi.org/10.1007/BF00206543

Willert, C. E., & Gharib, M. (1991). Digital particle image velocimetry. *Experiments in Fluids*, *10*(4), 181–193. https://doi.org/10.1007/BF00190388

Williams, M., & Houze, R. A. (1987). Satellite-observed characteristics of winter monsoon cloud clusters. *Monthly Weather Review*, *115*(2), 505–519. https://doi.org/10.1175/1520-0493(1987)115<0505:socowm>2.0.co;2

Winker, D. M., Hunt, W. H., & McGill, M. J. (2007). Initial performance assessment of CALIOP. *Geophysical Research Letters*, *34*, L19803. https://doi.org/10.1029/2007GL030135

Zhao, G., & Di Girolamo, L. (2007). Statistics on the macrophysical properties of trade wind cumuli over the tropical western Atlantic. *Journal of Geophysical Research*, *112*, D10204. https://doi.org/10.1029/2006JD007371